UKAEA FUS 396

UKAEA Fusion
(UKAEA/Euratom Fusion Association)

Comparison of theoretical models for scrape-off layer widths with data from COMPASS-D, JET and Alcator C-MOD

J W Connor, G F Counsell, S K Erents,
S J Fielding, B La Bombard, K Morel

35p.

March 1998

A CA

© UKAEA

UKAEA
Fusion

Culham Science Centre, Abingdon
Oxfordshire, OX14 3DB
United Kingdom
Telephone +44 1235 464131
Facsimile +44 1235 463647

Comparison of theoretical models for scrape-off layer widths with data from COMPASS-D, JET and Alcator C-MOD

J W Connor, G F Counsell, S K Erents, S J Fielding, B La Bombard*, K Morel+
UKAEA Fusion, Culham Science Centre
Abingdon, Oxon, OX14 3DB, UK
(UKAEA/Euratom Fusion Association)
*Plasma Fusion Center, Massachusetts Institute of Technology
Cambridge MA 02139, USA
+Imperial College of Science, Technology and Medicine
Prince Consort Road, London SW7 2BZ, UK

Abstract

The features of a number of theoretical models proposed to explain the cross-field transport in the scrape-off layer (SOL) are summarised. Simple balances of transport parallel and perpendicular to the magnetic field in the SOL allow one to derive predictions from these models for the power law scalings of the SOL width, Δ, with plasma parameters in the two cases of a collisionless and collisional SOL. Data on the SOL widths for a collisionless SOL from COMPASS-D and for a collisional SOL from JET and Alcator C-MOD are then used to test these models. Remarkably, the data from COMPASS-D, JET and Alcator C-MOD all favour the same small subset of these models. Furthermore, direct comparisons of the theoretical models for the cross-field thermal diffusivities with SOL data from JET and Alcator C-MOD provide some support for this finding. These 'best models' can be used to make predictions for MAST, the spherical tokamak under construction at UKAEA Culham, and for ITER.

1 Introduction

The power that heats a tokamak plasma must ultimately be exhausted from the confinement system. The fraction that is radiated is spread over the surrounding vessel and does not pose a serious problem. The remainder is transported across the closed flux surfaces of the tokamak to the plasma edge. The plasma edge can be defined by a limiter or magnetic separatrix and inside this, ie in the bulk or core plasma, profiles of density and temperature are determined by local perpendicular transport coefficients. Beyond this edge, in the scrape-off-layer (SOL), the profiles are determined by a competition between transport processes perpendicular and parallel to the magnetic field. The former are characterised by a perpendicular diffusion coefficient $D_\perp$ and the latter result from either parallel streaming in the collisionless regime $\nu < V_{\rm Th}/L_\parallel$ (where ν is a collision frequency, $V_{\rm Th}$ a thermal velocity and $L_\parallel$ the distance along the field line to a divertor plate or limiter), or parallel diffusion in the collisional regime, ie in the opposite limit $\nu > V_{\rm Th}/L_\parallel$. Neglecting sources and sinks

of plasma energy and particles, one can estimate the SOL width as

$$\Delta \sim \sqrt{\frac{D_\perp L_\parallel}{V_{\rm Th}}} \tag{1.1}$$

in the first case, and as

$$\Delta \sim \sqrt{\frac{D_\perp L_\parallel^2}{D_\parallel}} \sim L_\parallel \sqrt{\frac{D_\perp}{V_{\rm Th}\lambda_{\rm mfp}}} \tag{1.2}$$

in the second, where $\lambda_{\rm mfp}$ is a collisional mean free path. This width is significant as it plays a role in characterising the area of a divertor plate over which plasma energy is deposited. Because the parallel transport is so much faster than the perpendicular, the SOL width from eqn (1.1 or 1.2) is of the order of 1cm. In the case of proposed burning plasma experiments such as ITER the anticipated heat loads on the divertor target plates are a cause of great concern (and indeed, advanced schemes such as radiating and detached divertors are under investigation[1]). In reality much more complex physics is involved (neutral particles and ionisation, reflection at divertor plates etc) and the geometry is truly two-dimensional. In order to calculate realistic situations one needs to use complex two-dimensional edge physics codes such as B2-EIRENE, though these act rather as 'black boxes' and, as yet, benchmarking of them is limited. Nevertheless, progress in interpreting the results from these codes is being made, and more sophisticated versions of equations (1.1) and (1.2) are emerging[2].

However, the results will still depend on the values chosen for $D_\perp$. Typically, modellers choose $D_\perp$ (and $\chi_\perp$; we will generally use $D_\perp$ to represent both perpendicular particle and thermal diffusivities) to reproduce experimental data on Δ_n, the density SOL width (and, correspondingly, Δ_T, the temperature SOL width). This is usually achieved by expressing them as a number, say $D_\perp \sim 1{\rm m}^2{\rm s}^{-1}$, which may coincide numerically with the Bohm estimate. It is not clear that this is particularly useful for extrapolation to ITER or a power plant. What is needed is a physics basis for $D_\perp$ and its scaling with plasma parameters.

In Section 2 we review theoretical models for $D_\perp$ which can be used to estimate Δ through eqns (1.1, 1.2); we also include some marginal stability models that can be used to determine Δ directly. When the theoretical expressions for $D_\perp$ depend on gradients of density or temperature, one can estimate these using the SOL widths and solve self-consistently for them using eqns (1.1) or (1.2). In this way one can obtain predictions for Δ in terms of tokamak parameters: edge density n_a, major and minor radii R and a, respectively, magnetic field strength B, and edge temperature T_a, or heating power P. Simple theoretical models involving a single mechanism lead to power law scalings of the form

$$\Delta \propto n_a^{\lambda_n} R^{\lambda_R} a^{\lambda_a} B^{\lambda_B} q^{\lambda_q} P^{\lambda_P} \tag{1.3}$$

In Section 3 we compare the model predictions for Δ, of the form (1.3), with experimental data over the wide range of parameters available from the three tokamaks COMPASS-D, JET and Alcator C-MOD, in order to see if one can identify a suitable model for $D_\perp$ (or

Δ) for extrapolating to future devices such as ITER or MAST, the spherical tokamak under construction at Culham. Investigations of the SOL in JET and Alcator C-MOD have allowed the extraction of values for $\chi_\perp$ itself and in Section 4 we compare directly the scalings of these with the theoretical results from Section 2. In Section 5 we discuss the results and their implications for ITER and MAST and draw conclusions in Section 6.

2 Theoretical Models for SOL Widths

2.1 General comments

Models for turbulence in the SOL are based on familiar ones from core turbulence (ideal and resistive ballooning and interchange modes and drift waves) but with the added ingredients of effects arising from the presence of limiter or divertor plates, namely that field lines are open and there is a sheath boundary condition to be imposed at these plates.

Ideal ballooning or interchange modes can be unstable in the SOL at sufficient values of β because of regions of unfavourable curvature. However, the specific boundary conditions on the endplate allows ballooning and interchange instability [3] at lower β. This has been analysed in more detail in Ref 4. The authors of Ref 4 consider the stability of a flux tube; charge conservation in it can be expressed as:

$$\int_{\theta_1}^{\theta_2} \text{div} \left(\tilde{\text{J}}_{\text{curv}} + \tilde{\text{J}}_{\text{pol}}\right) qRd\theta + \tilde{J}_{||}(\theta_1) + \tilde{J}_{||}(\theta_2) = 0 \tag{2.1}$$

where $\tilde{\text{J}}_{\text{curv}}$ is the current perturbation due to curvature and $\tilde{\text{J}}_{\text{pol}}$ that due to the polarisation drift, while $\tilde{J}_{||}(\theta_{1,2})$ are the parallel currents through the sheaths at the ends θ_1 and θ_2 of the flux tube (the short stabilising lengths in a divertor chamber are neglected). These parallel currents are obtained from an expression for the current at the endplate:

$$J_{||} = ne\left[V_{\text{Thi}} - V_{\text{The}} \exp\left(-\frac{e\Phi}{T_e}\right)\right] \tag{2.2}$$

where Φ is the electrostatic potential. The equilibrium potential Φ_0 adjusts to ensure losses at the ends are ambipolar, ie

$$neV_{\text{Thi}} = neV_{\text{The}} \exp\left(-\frac{e\Phi_0}{T_e}\right) \tag{2.3}$$

so that, when there is a potential perturbation ϕ [5],

$$\tilde{J}_{||}(\theta_{1,2}) = -\frac{ne^2}{T_e}\phi(\theta_{1,2})V_{\text{Thi}} \tag{2.4}$$

This current response, which is stabilising, is much less than the standard response to resistivity in the core by a factor $(m_e/m_i)^{1/2}(k_{||}V_{\text{The}}/\nu_e)$, where $k_{||}$ is the parallel wave number of a mode. Furthermore, new, strongly unstable, electron temperature gradient instabilities arise due to the presence of this sheath boundary condition.

2.2 Ideal MHD ballooning and interchange instabilities

The simplest model by Peng[6] assumes that, due to unfavourable curvature regions, the SOL is at marginal stability to ideal ballooning modes. Balancing the release of pressure gradient energy due to unfavourable curvature against the field line bending energy, assuming line-tying at the divertor plates, one obtains a pressure decay length Δ_p

$$\Delta_p \sim \frac{\beta_b L_{\|}^2}{R} \tag{2.5}$$

where $\beta_b \simeq 2\mu_0 p_b/B^2$, with the subscript b denoting the SOL region. Some experimental evidence for this scaling has been cited by Peng[6].

Pogutse and Kerner[7] have introduced a simplified version of the divertor geometry in the SOL to calculate the critical ideal β for interchange modes, finding

$$\hat{\beta}_{\rm crit} \equiv \frac{\beta_{b\rm crit} L_{\|}^2}{\Delta_p R} \sim 5.6 \tag{2.6}$$

A more realistic analysis[8] yields an analytic estimate

$$\hat{\beta}_{\rm crit} \equiv \frac{\beta_{b\rm crit} R q^2(\pi)}{\Delta_{px}} = 2 \tag{2.7}$$

where the safety factor $q_{95} \simeq 3q(\pi)$ and Δ_{px} is the pressure gradient length at the X-point (numerical calculations indicate values smaller by a factor 3).

2.3 Effects of sheath and bulk plasma resistivity on ballooning and interchange modes

Garbet et al[4] have considered the effect of sheath resistance (or 'end loss') on the ideal interchange mode. If the curvature effects are destabilising, which occurs if

$$H(\theta)|_{\theta_1}^{\theta_2} > 0 \tag{2.8}$$

where $H(\theta) = (1+s)\sin\theta - s\theta\cos\theta$ with $s = d(\ell nq)/d(\ell nr)$, then the maximum growth occurs for a radial wave number $k_r = 0$, although this growth is only a weak function of k_r for $k_r < k_\theta$, where k_θ is the poloidal wave number. The most unstable modes are found when the end loss can be neglected, ie

$$k_\theta \rho_i > \left[\frac{2L_p}{q^2 R H(\theta)|_{\theta_1}^{\theta_2} G(\theta)|_{\theta_1}^{\theta_2}}\right]^{1/4} \sim 0.1 \tag{2.9}$$

where L_p is the pressure gradient scale-length, $G = s^2\theta^3/3 + \theta$, and the corresponding growth rate is

$$\gamma \sim \frac{V_{\rm Thi}}{R}\left[\frac{2RH(\theta)|_{\theta_1}^{\theta_2}}{L_p G(\theta)|_{\theta_1}^{\theta_1}}\right]^{1/2} \tag{2.10}$$

In the opposite case[3]

$$\gamma \sim k_\theta q \rho_i H(\theta)|_{\theta_1}^{\theta_2} \omega_{*e} \tag{2.11}$$

where ω_{*e} is the electron diamagnetic frequency and ρ_i the ion Larmor radius. An estimate $D_\perp \sim \gamma/k_\theta^2$ using equations (2.9) and (2.10) is

$$D_\perp \sim \frac{qV_{\rm Thi}}{L_p} \rho_i^2 H(\theta)|_{\theta_1}^{\theta_2} \tag{2.12}$$

where, for a double null divertor, $H \sim 6$. The turbulence is large scale, $k_\perp \rho_i \sim 0.1 (k_\perp$ is the wave number perpendicular to the magnetic field), there is a large phase shift ($\sim 60°$) between density and potential fluctuations and the phase velocity along the field lines is large.

The instability mechanism in Ref 4 has been extended to incorporate bulk plasma resistivity as well as the endplate 'resistivity'[9]. The result is, in practical units (ie T in eV and all other quantities in SI),

$$D_\perp = \frac{2TL_\parallel}{B^2|L_p|R} \left\{ \frac{7.2\ 10^{-5} T^{1/2} A^{1/2}}{V} + 2.1\ 10^{-5} \frac{nL_\parallel \ell n\lambda}{T^{3/2}} \right\} \tag{2.13}$$

Here the first term is the sheath contribution[4], while the second is due to the bulk plasma resistivity. The second dominates at lower temperatures. The quantity $V = (m_i/4\pi m_e)^{1/2}$ $\exp(-e\Phi_0/T)$ represents the ratio of equilibrium electron to ion saturation currents (it can be unity), A is the atomic mass number and $\ell n\lambda$ the Coulomb logarithm.

Pogutse and Kerner have included the effects of both sheath and bulk plasma resistivity, together with losses of plasma along the field lines, on the interchange modes[7], and find them unstable below $\hat{\beta}_{\rm crit}$ (eqn 2.6). A mixing length estimate for cross-field transport yields, in the free streaming (collisionless) limit,

$$D_\perp \sim \frac{c^2}{\omega_{pi}^2} \left(\frac{\hat{\beta}}{\hat{\beta}_{\rm crit}} \right)^2 \frac{c_s}{L_\parallel} \tag{2.14}$$

for a single null divertor (a linear dependence on $\hat{\beta}/\hat{\beta}_{\rm crit}$ appears in the double null case), where ω_{pi} is the ion plasma frequency $\sim (ne^2/m_i\epsilon_0)^{1/2}$ and c_s is the sound speed $(T_e/m_i)^{1/2}$. Near $\hat{\beta} \sim \hat{\beta}_{\rm crit}$

$$D_\perp \sim \frac{c^2}{\omega_{pi}^2} \frac{c_s}{L_\parallel} \tag{2.15}$$

For bulk Spitzer resistivity η,

$$D_\perp \sim (\eta/2\mu_0)\hat{\beta}/\hat{\beta}_{\rm crit} \tag{2.16}$$

similar to the second term in eqn (2.13), for both single (SND) and double null (DND) divertors.

Pogutse et al[10] have also considered the non-linear evolution of the resistive interchange instabilities in the SOL. Results similar to eqn (2.13) were found: for bulk resistivity

$$D_\perp \sim \frac{L_\parallel^2}{L_p R}\nu_{ei}\rho_e^2 \tag{2.17}$$

where ν_{ei} is the electron-ion collision frequency and ρ_e the electron Larmor radius; for sheath resistivity

$$D_\perp \sim \frac{L_\parallel}{L_p R}c_s\rho_s^2 \tag{2.18}$$

where ρ_s is the ion Larmor radius evaluated at the electron temperature. Reference 10 provides self consistent expressions for $D_\perp$ and $\Delta \sim L_p$, using eqns (1.1) and (1.2) to determine Δ, in practical units.

A more careful analysis of the sheath boundary condition, considering the perturbations in n and Φ in eqn (2.2), and drift effects, was given in Ref 11. The resulting 'mixing length' estimates for $D_\perp$ were

$$D_\perp \sim \frac{\rho_s^2 c_s L_\parallel}{L_p}\hat{\beta}^\nu \quad , \quad \hat{\beta} = \frac{L_\parallel^2}{L_p R}\beta \tag{2.19}$$

for the resistive interchange, where $\nu = 0$ for double null and $\nu = 1$ for single null divertors, and

$$D_\perp \sim \frac{\rho_s^2 c_s}{L_n}\left(\frac{L_\parallel}{L_n}\right)^{1/3} \tag{2.20}$$

for the drift instability, where L_n is the density gradient length. The two expressions (2.19, 20) are comparable for a double-null divertor, but the drift instability dominates for a single-null configuration. It is interesting to note that Cordey et al[12] have shown that the direction of parallel current, $j_\parallel$, in the SOL affects the sheath resistance for interchange modes in a SND. As a result the predicted $D_\perp$ increases with $j_\parallel$ by a factor 2-4. Experimentally $j_\parallel$ is found to be positive for ion-∇B drifts away from the X-point; thus Δ increases in this situation.

Another instability that can arise in the SOL is due to shear of the $\boldsymbol{E} \times \boldsymbol{B}$ frequency, ω_E, along the magnetic field line [13]. This variation is a consequence of the variation of the electrostatic potential Φ_0 along the field towards the divertor plate. Together with sheath boundary conditions this can destabilise the shear Alfvén wave. To compare the strength of this instability with the curvature driven ones, it is necessary to consider a self-consistent treatment of the divertor geometry which controls the respective driving gradients of the two instabilities. Reference 14 presents such a treatment based on a large aspect ratio, 'two-wire' model for the tokamak divertor geometry, with a Braginskii two-fluid model to determine the equilibrium variation of Φ_0 from Ohm's Law. This is controlled by the variation of T_e and two limits for parallel transport of T_e in the divertor are considered: collisionless, with T_e approximately constant along the field, and collisional. The stability problem is solved in the high n (n is the toroidal mode number) ballooning limit including finite Larmor radius (FLR) effects and electron resistivity or inertia. The presence of the X point enhances the effects of FLR and the equilibrium shear in ω_E.

The MHD interchange mode is only weakly ballooning and is found to be stabilised by line tying at low n and FLR at high n, with maximum growth for $n \sim 50$ typically. The interchange drive dominates over the drive due to the sheath. The collisionality of the divertor has little effect and resistivity (which plays a role for $n > n_r$ with $n_r \sim 10$ - 50) only a minor qualitative impact. The ω_E shear mode exists in the collisional divertor and is localised between divertor and X-point, especially at high n. This mode is not stabilised at high n by fluid FLR effects since $\omega_E \propto n$. Thus, while the interchange mode dominates for lower n, the ω_E shear mode persists at high n. Indeed, estimating $D_\perp \sim \gamma/k_\perp^2$, the contribution from the ω_E shear mode saturates at high n, dominating the MHD interchange for $n \gtrsim 200$. Resistivity is found to enhance the growth rate of the ω_E shear mode by a factor $\lesssim 3$. Including gyro-kinetic effects ($k_\perp \rho_i \sim 1$) heuristically, does suppress the high n contribution to $D_\perp$; the MHD interchange contribution dominates for $n < 100$.

The MHD interchange mode drive gives rise to a contribution to $D_\perp$, on choosing the maximising value of n, of the form

$$\frac{D_\perp^{(1)}}{D_{\text{Bohm}}} = 3.4 \times 10^{-4} \frac{A^{1/2}}{Z^{3/2}} \left(\frac{s_2 q_2}{s_1 q_1}\right)^2 \frac{n_e}{n_{ep}} \frac{T_i}{T_e} \frac{L_E T_{ep}^{1/2}}{RBL_p} \tag{2.21}$$

in units (m, eV, T), where Z is the ionic charge.

Here parameters with the suffix p are at the divertor plate, otherwise at the mid-plane. The suffix 1 is at a poloidal angle opposite the X-point, suffix 2 in the vicinity of the X-point and $(s_2 q_2)/s_1 q_1 \sim 7$; L_E is the parallel gradient length of ω_E. Reference 14 also gives contributions from the sheath drive to the MHD mode, although it was found to be less important for the cases examined:

$$\frac{D_\perp^{(2)}}{D_{\text{Bohm}}} = 2.9 \times 10^{-3} \frac{A^{1/2}}{Z^{1/2}} \left(\frac{s_2 q_2}{s_1 q_1}\right)^2 \left(\frac{n_e}{n_{ep}}\right)^{1/3} \frac{L_E^{5/3}}{L_\parallel^{4/3}} \frac{T_e^{1/3} T_{ep}^{1/6}}{B L_{Te}^{4/3}} \tag{2.22}$$

where L_{Te} is the electron temperature gradient length. Finally, for the ω_E shear mode,

$$\frac{D_\perp^{(3)}}{D_{\text{Bohm}}} = 1.4 \times 10^{-3} \frac{A^{1/2}}{ZB} \frac{L_E}{L_\parallel} \frac{T_i^{1/2}}{L_{Te}} \tag{2.23}$$

Typically $D_\perp^{(1)}$: $D_\perp^{(2)}$: $D_\perp^{(3)}$ are in the ratios 13:5:0.02 and the respective scalings are

$$D_\perp^{(1)} \propto (BL)^{-1} D_{\text{Bohm}} \tag{2.24}$$

$$D_\perp^{(2)} \propto (BL)^{-1} (RT/L)^{1/3} D_{\text{Bohm}} \tag{2.25}$$

$$D_\perp^{(3)} \propto (BL)^{-1} T^{1/2} D_{\text{Bohm}} \tag{2.26}$$

where L is a typical SOL gradient length.

2.4 Drift resistive ballooning mode turbulence

The resistive ballooning modes can be unstable even in the core plasma, so before discussing the effects of endplates and open field lines, it is appropriate to describe the characteristics

of the resulting turbulence in the plasma edge region. The most recent version of the linear theory of these modes has been given by Novakovskii et al[15]. It is characterised by two parameters

$$\hat{m} = k_\theta L_0 \quad , \quad \alpha = \frac{\rho_s c_s}{L_n L_0 \gamma_o} \tag{2.27}$$

where the characteristic scale length is

$$L_0 = 2\pi q \left(\frac{2R}{L_n}\right)^{1/4} \left(\frac{2\nu_{ei} R \rho_s}{\Omega_e}\right)^{1/2} \tag{2.28}$$

with Ω_e the electron cyclotron frequency, and the characteristic growth rate is

$$\gamma_0 = c_s \left(\frac{2}{RL_n}\right)^{1/2} \tag{2.29}$$

Since $\alpha = \omega_{*e}/\hat{m}\gamma_0$, it characterises diamagnetic effects. Typically, $L_0 \sim 0.25 - 0.75$cm, $\alpha \sim 0.5$ for L-mode and Ohmic plasmas and 1.5 for H-mode.

For small $\hat{m}$ there is the conventional weakly ballooning mode which becomes almost stable for $s \gtrsim 1$, ie near the plasma edge. However, there is also a more strongly ballooning mode which matches onto the ballooning mode with ideal growth rate

$$\gamma \sim \gamma_0 \tag{2.30}$$

which exists for $\hat{m} \gg 1$. Furthermore, there is a transition from resistive ballooning to drift modes when $\alpha > 1$. Long wavelength resistive ballooning modes are stable for $\alpha > 1.5$, while short wavelength ones would be stabilised by realistic values of viscosity. Three dimensional non-linear fluid simulations have been carried out by Zeiler et al[16,17]. In the regime of low α ($\alpha < 1$) it is found that there is a large asymmetry of turbulence and transport between inboard and outboard sides. For cases with $0.5 < \alpha < 1.0$

$$D_\perp = c(\theta) D_0 \tag{2.31}$$

where the characteristic diffusion coefficient is

$$D_0 = \frac{L_\parallel^2}{RL_n} \nu_{ei} \rho_e^2 \propto \frac{nq^2}{B^2 T^{1/2}} \frac{R}{L_n} \tag{2.32}$$

and $c(0) \simeq 0.07$, $c(\pi) \simeq 0.035$. The density and potential fluctuations also vary by factors ~ 2 from inside to out. For higher values of α, despite the stabilisation of the linear modes, the turbulence remains strong due to a non-linear instability. It has a weakly ballooning character, propagates in the electron direction and has a larger transverse correlation length. In the limit that curvature is unimportant, the resulting non-linearly unstable turbulent transport can be scaled as

$$D_\perp = \hat{D} f(\hat{\rho}) \tag{2.33}$$

where

$$\hat{D} = D_0 \left(\frac{\alpha^2}{s}\right)^{2/3} \tag{2.34}$$

and

$$\hat{\rho} = \left(\frac{L_n}{R}\right)^{1/2} (\alpha s)^{2/3} \equiv \frac{\rho_s}{L_\perp} \tag{2.35}$$

Here $L_\perp = (\rho_s^2 L_\parallel^2 \nu_{ei}/2s^2\Omega_e L_n)^{1/3})$ is the characteristic perpendicular scale of the drift wave turbulence. The factor f is found to drop from $f = 0.045$ for $\hat{\rho} = 0$, to zero for $\hat{\rho} \sim 0.12$, where the non-linear instability dies away. The inclusion of $T_i \neq 0$ results in $\hat{\rho}$ being multiplied by a factor $(1+\tau)^{1/2}$ and α divided by the same factor, where $\tau = T_i/T_e$. Allowing for electron temperature perturbations $\tilde{T}_e$ makes some quantitative changes to these results[18]. Thus parallel electron thermal diffusivity, $\chi_{\parallel e}$, suppresses the ∇T_e drive except at low T_e in the resistive ballooning regime; increasing α also loses the ∇T_e drive. Furthermore, inclusion of $\tilde{T}_e$ provides additional dissipation, so that the fluxes fall sharply with T_e. In the drift wave regime ($\alpha > 1$) the particle flux is suppressed by a factor 4 and the heat flux by a factor 2 due to including $\tilde{T}_e$. One finds f in eqn (2.33) can be written

$$f \propto \hat{\rho}^{-4} \tag{2.36}$$

independent of $\eta_e (= d(\ell n T_e)/d(\ell n n))$. Thus

$$D_\perp \propto \frac{(Rq)^{10/3} n^{5/3}}{B^2 T_e^{11/6} L_n^{8/3}} \tag{2.37}$$

in this regime. However, a proper understanding requires a treatment of the interface between the SOL and core plasma. A start on this has been made in Ref 19, where the SOL region is modelled independently of the core and boundary conditions at a limiter are introduced. Thus using equation (2.4), a new parameter λ is introduced

$$\lambda = \left(\frac{m_e}{m_i}\right)^{1/2} \frac{\nu_{ei} q R}{V_{\mathrm{The}}} \tag{2.38}$$

In terms of practical units (10^{19} m^{-3}, m, eV)

$$\lambda = 20 \frac{n_{19} q R}{T^2} Z_{\mathrm{eff}} \tag{2.39}$$

so that typically $\lambda \simeq 0.01$ for TFTR, 0.1 for DIII-D and 0.5 for ITER.

For $\hat{m} \gg 2\pi$ one recovers the strong ballooning result (2.29). In the other limit, $\hat{m} \ll 2\pi$, and with $\lambda \ll 1$ there is a flute-like mode driven by the geodesic curvature. For $\hat{m}^2 s^{1/2} \gg 4\pi^2 \lambda$ the SOL mode is more unstable than the core plasma mode but is stabilised by FLR if $\hat{m} > 2/(\pi s \alpha)$. In the opposite limit

$$\gamma = \frac{\hat{m}^2 s}{8\pi\lambda} \gamma_0 \tag{2.40}$$

This leads to a mixing length estimate for the diffusion coefficient

$$D_\perp \sim \frac{s}{8\pi\lambda} \gamma_0 L_0^2 \propto \frac{T^{3/2} q}{L_n B^2} \tag{2.41}$$

which exceeds equation (2.31) and resembles (2.12). For $\lambda \gg 1$ the mode must vanish at the endplates and this line-tying weakens the growth rate. For $\hat{m} \gg 1$ the modes are strongly ballooning and unaffected by the endplates. Even for small $\hat{m}$, finite $\alpha(\sim 1)$ has a strong stabilising influence.

The impact of electromagnetic effects (namely the self consistent magnetic fields induced by the perturbed plasma currents) on drift wave transport has been considered by Chankin[20]. This has the consequence that one must calculate the cross-field transport as the difference between the motion of plasma and the magnetic surfaces, which is proportional to the plasma resistivity[21]. Chankin finds this becomes significant when the collisional skin-depth becomes comparable with the fluctuation scale-length. As a result

$$D_\perp \simeq \eta/2\mu_0 \propto T_e^{-3/2} \tag{2.42}$$

beyond this point. The condition for this can be obtained by equating a typical drift wave diffusivity

$$D_\perp \sim \frac{\omega_{*e}}{k_r^2} \tag{2.43}$$

to eqn (2.42). Using eqn (1.1) to determine L_n in the SOL and choosing $k_r \propto 1/\rho_s$, one finds the condition for the collisional skin-depth to play a role is given by a critical value of the quantity

$$\frac{T_e^{13/8}(T_e+T_i)^{3/8}}{BZ_{\text{eff}}^{3/4}(qR)^{1/4}} \tag{2.44}$$

In the collisionless case, when $k_r \sim \omega_{pe}/c$ (the inverse collisionless skin-depth), one has the condition

$$\beta > \beta_{\text{crit}} \sim 2(k_r\rho_s)^2\frac{m_e}{m_i} \tag{2.45}$$

and a corresponding diffusion coefficient

$$D_\perp \sim \left(\frac{c}{\omega_{pe}}\right)^2 \frac{c_s}{L_n} \propto \frac{T_e^{1/2}}{nL_n} \tag{2.46}$$

The transport associated with the electromagnetic drift-Alfvén instability has been explored by Pogutse et al[22] as a potential explanation of the L-H transition. Using a collisionless gyro-kinetic ion and fluid electron model, these authors obtained expressions for the turbulent transport coefficients; these are based on dimensional arguments and quasi-linear theory. The expressions are characterised by a collisionality parameter $\nu_n = (\nu_{ei}L_\parallel/V_{\text{The}})$ $(L_p/L_\parallel)^{1/2}(m_i/m_e)^{1/4}$ and a β parameter $\beta_n = (m_i/m_e)^{1/2}\ \beta(L_\parallel/L_p)$. In their lower β, L-mode, limits they can be expressed in a somewhat simplified fashion as

$$D_\perp \sim \frac{c_s\rho_s^2}{L_p^{3/2}}L_\parallel^{1/2}\left(\frac{m_e}{m_i}\right)^{1/4} \quad , \quad \nu_n, \beta_n \ll 1 \tag{2.47}$$

and

$$D_\perp \sim \frac{c_s\rho_s^2}{L_p^{4/3}}L_\parallel^{1/3}\left(\frac{\nu_e L_\parallel}{V_{\text{The}}}\right)^{1/3}\left(\frac{m_e}{m_i}\right)^{1/6} \tag{2.48}$$

2.5 Temperature Gradient Instabilities

If one allows an electron temperature perturbation, $\tilde{T}_e$, in the boundary condition (2.4), then [23]

$$\tilde{J}_{\|}(\theta_{1,2}) = \frac{\epsilon e n V_{\rm Thi}}{2\sqrt{\pi}} \left[\frac{e\phi}{T_e} - \left(\frac{e\Phi_0}{T_e} + \frac{1}{2} \right) \frac{\tilde{T}_e}{T_e} \right] \tag{2.49}$$

where $\epsilon \ll 1$ represents the absorption of ions at the endplates, and more accurate numerical factors than in equation (2.4) have been introduced. The equilibrium potential Φ_0 is given by $\Lambda T_e/e$, where the parameter $\Lambda = \ell n(V_{\rm Thi}/V_{\rm The}) \sim 4$; this parameter plays a crucial role in the theory. Using a simple $\tilde{\mathbf{E}} \times \mathbf{B}$ convection model for $\tilde{T}_e$, one finds an instability even in the absence of curvature effects. Indeed it is much more important than that discussed in Ref 4. It has a maximum growth rate γ_m

$$\gamma_m \simeq 0.4 \left(\frac{\Lambda^2 T_e}{\tau_{\|} m_i L_T^2} \right)^{1/3} \propto \frac{V_{\rm Thi}}{L_{\|}} \left(\frac{T_e}{T_i} \right)^{1/3} \left(\frac{\epsilon \Lambda^2 L_{\|}^2}{L_T^2} \right)^{1/3} \tag{2.50}$$

where $\tau_{\|} = \sqrt{\pi} L_{\|}/\epsilon V_{\rm Thi}$ is the particle lifetime along the magnetic field and L_T the temperature scale length. This maximum growth rate occurs at

$$k_\theta \rho_i \sim \left(\frac{T_i}{T_e} \right)^{2/3} \left(\frac{\epsilon}{\Lambda} \frac{L_T}{L_{\|}} \right)^{1/3} \tag{2.51}$$

The instability leads to a mixing length estimate for transport given by

$$D_\perp \simeq 0.1 \left(\frac{T_e}{T_i} \right)^{5/3} \left(\frac{\Lambda V_{\rm Thi} \tau_{\|}}{L_T} \right)^{4/3} \frac{\rho_i^2}{\tau_{\|}} \tag{2.52}$$

For a typical example ($\Lambda \sim 4, B = 3$ T, $L_{\|} \simeq 20$m, $T = 30$eV), eqns (1.1) and (2.50) imply $L_T (\sim \Delta_T) \sim 2$cm, while $k_\theta \rho_i \sim 0.2$ and a mixing length estimate yields $\tilde{n}/n \sim 1/k_\theta L_T \sim 0.1$. Two fluid FLR effects are found to improve stability, but are numerically weak.

A more detailed electromagnetic, Braginskii two-fluid treatment of this instability has been given.[24]. This also includes the effects arising from differences in plasma parameter values between mid-plane and endplates, (eg n and n_p for the density, where we again label the plates by the suffix p), secondary emission of electrons due to electron and ion bombardment (with coefficients γ_e and γ_i, respectively) and finite $k_{\|}$ effects. Although the sheath boundary conditions on the energy flux at the endplates introduce a number of atomic physics parameters, these have a negligible effect on the instability; in fact the only atomic physics parameter of any significance is found to be γ_i. The resulting mixing length diffusivity is, for $k_{\|} \simeq 0$,

$$D_\perp \simeq 0.1 \frac{c_s \rho_s^2}{L_{Te}} \Lambda^1 \left[\frac{\Lambda^1 L_{\|} c_{sp} n}{2 L_{Te} c_s n_p (1+\gamma_i) Z} \right]^{1/3} \tag{2.53}$$

for $\delta = (T_i/T_{ep})(L_{Te}/L_{pi}\Lambda^1)/Z \ll 1$ and

$$D_\perp \simeq \frac{1}{3}\frac{c_{sp}\rho_s^2}{L_{Te}}\Lambda^1 \left[\frac{T_i L_{\|} c_{sp} n}{2T_{ep}L_{pi}c_s n_p(1+\gamma_i)Z}\right]^{1/3} \tag{2.54}$$

for $\delta \gg 1$. Here $c_{sp} = (T_{ep}/m_i)^{1/2}$ and

$$\Lambda^1 = \Lambda + (T_{ip}/2T_{ep})\left[1 - L_{Tep}/L_{Tip}\right](1 + T_{ip}/T_{ep}) \tag{2.55}$$

The effect of finite $k_{\|}$ is parameterised by the quantity

$$K = (1+\gamma_i)Z\left(\frac{\beta_p n_p}{2n}\right)^{1/2}\nu^{-2/3} \tag{2.56}$$

where

$$\nu = \frac{2n_p c_s L_{Te}(1+\gamma_i)}{n\Lambda^1 c_{sp} L_{\|}}\ ,\ \beta_p = \frac{2\mu_0 n_p(T_{ep}+T_{ip})}{B^2} \tag{2.57}$$

Its effect is only moderate for typical present day experiments, but can enhance $D_\perp$ for ITER parameters. Reference 24 also expresses the resulting $D_\perp$ in meaningful units:

$$D_\perp \simeq \frac{2.3}{\hat{L}_{Te}^{4/3}}\hat{T}_{ep}^{3/2}\left(\frac{\Lambda^1}{4}\right)^{4/3}\hat{L}_{\|}^{1/3}\left(\frac{1.5}{(1+\gamma_i)Z}\right)^{1/3}A^{1/2}\frac{1}{\hat{B}^2}\left(\frac{n}{n_p}\right)^{1/3}\left(\frac{2T_e}{T_e+T_i}\right)_p^{1/6}G \tag{2.58}$$

where $\hat{T}_{ep}$ is in units of 25eV, $\hat{L}_{Te}$ in cm, $\hat{L}_{\|}$ in 40m, $\hat{B}$ in 2T. The value of G depends on δ and K: $G \sim 1$ for $\delta = K = 0$; $G \sim 2$ for $\delta = 1$, $K = 0$ (typical for DIII-D); $G \sim 1$ for $\delta = 1$, $K = 2$ due to a cancellation; $G = 3$ for $K \gg 1$ (typical of a power plant). Reference 24 considers particle and energy balances in detail to determine L_n, L_{Te}, L_{Ti} self-consistently, leading to forms for γ, D, $k_\theta\rho_s$, $\tilde{T}_e$ etc. (It should be noted that the energy lifetime along the field is $L_{\|}/c_s\Lambda$, while that for particles is $L_{\|}/c_s$). A consequence is that $D_\perp \sim (\rho_s/L_{\|})^{1/5}\Lambda^{6/5}D_{\text{Bohm}}$, ie comparable to D_{Bohm}, so that Δ_T can be many ρ_i.

Fluid simulations of the turbulence associated with the ∇T_e instability have been carried out in the electrostatic limit using the geometry of Ref 24, but without magnetic shear[25]. The effects of ∇T_i are retained. It is found that the saturated amplitudes of ϕ and $\tilde{T}_e$ are somewhat above mixing length estimates, with the heat fluxes somewhat below them. Thus the electron thermal diffusivity is given by

$$\chi_e \simeq 0.02\frac{3c_s\rho_s^2}{2L_{Te}}\Lambda\left[\frac{\Lambda L_{\|}}{2\sqrt{1+T_e/T_i}L_{Te}}\right]^{1/3} \tag{2.59}$$

For typical DIII-D SOL parameters, $e\phi/T_e \sim 40\%$, $\tilde{T}_e/T_e \sim 15\%$ and $\chi_e \sim 0.3\text{m}^2\text{s}^{-1}$, while the phase shift between ϕ and $\tilde{T}_e$ is a factor 0.7. The fluctuations are peaked near the last closed flux surface and penetrate into the edge plasma in the long wavelength regime. The weaker transport is associated with an inverse cascade of the turbulence, so that turbulent

and equilibrium scales merge. (This effect justifies the approach of Ref 26 discussed below.) Self-consistent simulations in which T_e and L_{Te} are determined in terms of the heat flux from the core were also carried out. T_e is found to fall exponentially in the SOL with $L_{Te} \sim 1.0$cm typically, comparable to experimental values; this is insensitive to the heating power.

The turbulence calculations of Ref 25 showed an inverse cascade of energy to long wavelengths, blurring the distinction between turbulent and equilibrium scalelengths and making the concept of a turbulent diffusivity inappropriate. It has been shown in Ref 26 how a more general approach can be used to avoid making the separation-of-scales assumption needed for the calculation of a local transport coefficient. The model for the SOL turbulence used in Ref 25 has similar properties to the paradigmatic Hasegawa-Wakatani drift wave model. Thus its non-linear interactions conserve two quantities, energy E and enstrophy Ω:

$$E = \frac{m_i}{2}\int dV \tilde{\boldsymbol{V}}_E^2 \quad , \quad \Omega = \frac{m_i}{2}\int dV (\nabla \times \tilde{\boldsymbol{V}}_E)^2 \tag{2.60}$$

where $\tilde{\boldsymbol{V}}_E = \boldsymbol{E} \times \boldsymbol{B}/B^2$; while energy cascades inversely to long wavelength, enstrophy cascades to short wavelength. In terms of the overall energy balance, heat flows in from the core plasma (alternatively one can consider ∇T_e to drive the fluctuations) and is damped at long wavelengths on the endplates and at short wavelengths by viscosity; enstrophy also is dissipated by viscosity at short wavelengths. Thus the injection of energy and associated entrophy to drive instabilities locally in wave number space, causes a forward cascade of Ω. This drives an inverse cascade of E, which continues until Ω is depleted; at this point non-linear interactions cease and E becomes part of the equilibrium. However, the boundary conditions on the energy prevent this being a state of zero enstrophy. Thus the equilibrium can be obtained by minimising the enstrophy for given energy. This results in the variational principle

$$\delta(\Omega_0 + \lambda^2 E_0) = 0 \tag{2.61}$$

where Ω_0 and E_0 are the equilibrium values of Ω and E respectively, and λ^2 is a Lagrange multiplier. This condition leads to the following minimum enstrophy condition on the equilibrium $\boldsymbol{E} \times \boldsymbol{B}$ flow in the SOL

$$\nabla^2 \boldsymbol{V} = \lambda^2 \boldsymbol{V} \tag{2.62}$$

For a toroidally limited SOL this has solution

$$V_\theta(r) = V_0 e^{-\lambda(r-a)} \tag{2.63}$$

The equilibrium endplate boundary condition (2.2) with $J_{||} = 0$ implies

$$T_e(r) = \frac{-eB}{\lambda\Lambda} V_\theta(r) \tag{2.64}$$

ie this is obtained without explicitly solving for the thermal transport! In the core the SOL flow is damped by viscosity so that

$$V = V_0 \exp\left[-\sqrt{\frac{D}{\mu}}(a-r)\right] \quad r < a \tag{2.65}$$

where D and μ are the coefficients of kinematic viscosity and drag. Overall energy balance can be used to determine V_0 in terms of λ

$$V_0 = \frac{\sqrt{2\pi} L_{\|} Q_e \Lambda \lambda^2}{2(2+\Lambda) n_e V_{\rm Thi} eB} \tag{2.66}$$

where Q_e is the electron heat flux from the core. Finally, dimensional analysis can be used to write

$$\lambda = \left(\frac{n_e \Omega_i^3 m_i}{Q_e L_{\|}} \right)^{1/4} \tilde{\lambda}(\Lambda) \tag{2.67}$$

where $\tilde{\lambda}$ is an unknown function of Λ. It is interesting to note that eqns (2.64 - 2.67) determine an effective χ_e

$$\chi_e \propto \frac{\rho_i}{L_{\|}} \frac{T_e}{eB} \tag{2.68}$$

2.6 Other Models

In this subsection we conclude the physics based models with some miscellaneous ones. The first is to assume transport proceeds by charge-exchange collisions, yielding

$$D_\perp \sim \nu_{\rm cx} \lambda_{\rm cx}^2 \propto \frac{T^{1/2}}{n} \tag{2.69}$$

The second is the ubiquitous Bohm coefficient,

$$D_\perp \sim \frac{T_e}{eB} \tag{2.70}$$

Two other arguments based on dimensional arguments can be advanced. If one takes the collisionless skin-depth (c/ω_{pe}) as a step-length and the transit time along the field line to the divertor ($L_{\|}/c_s$) as a time-step in a random walk argument, then

$$D_\perp \sim \frac{c_s}{L_{\|}} \left(\frac{c}{\omega_{pe}} \right)^2 \sim \frac{T^{1/2}}{nRq} \tag{2.71}$$

Another model is to assume that the level of turbulent fluctuations, ϕ, and their perpendicular wave number, $k_\perp$, satisfy a balance of the $\tilde{\boldsymbol{E}} \times \boldsymbol{B}$ circulation frequency ($\Omega \sim k_\perp^2 \phi / B$) and the transit frequency along the field lines ($c_s/L_{\|}$). If we suppose the turbulent fluctuations also satisfy $\phi \sim T_e/e$ and that the fluctuation spectrum is isotropic with $k_\perp \sim 1/\Delta$, then

$$\Delta \sim (\rho_s L_{\|})^{1/2} \tag{2.72}$$

For completeness we include a frequently used model, but which has no physics basis,

$$D_\perp \sim \text{ constant} \tag{2.73}$$

3 Comparisons of theoretical predictions for the SOL widths with experimental data

3.1 SOL width scalings

In this section we compare the scalings for Δ corresponding to the theoretical cross-field diffusivities discussed in Section 2 with respect to experimental data from COMPASS-D, JET and Alcator C-MOD. In order to do this we use eqns (1.1) and (1.2) and power balance to derive predictions for the scaling of Δ with various tokamak parameters (ie n, P, B, a, R, q) for those theoretical models. Since the theoretical diffusivities often contain perpendicular gradient lengths (L_n, L_p, L_{Te}) these too must be determined self-consistently. Density transport along the field lines takes place at the sound speed and thus one might expect that $L_n (\sim \Delta_n)$ is always controlled by eqn (1.1), a 'collisionless' scaling. As a result one would have $L_n \lesssim L_{Ti}$ since L_{Ti} is controlled by convection in the collisionless case and ion parallel thermal diffusivity in the collisional case. However, in the collisional limit the heat flux to the target plates sets a temperature SOL width determined by electron parallel thermal conduction, which dominates convection at the sound speed provided the collisionality parameter is not too high: $\nu_{*e} < (m_i/m_e)^{1/2}$. In this situation strong recycling takes place near the target, since the incident energy is high enough to ionise neutrals. As a result the density and electron temperature SOL widths L_n and L_{Te} would tend to be comparable and both given by eqn (1.2) in the collisional limit. We therefore suppose that L_n, L_{Te} and L_p are all controlled by eqn (1.1) in the collisionless case, $\nu_{*e} < 1$, and by eqn (1.2) for the collisional case, $\nu_{*e} > 1$. However, we find little significant change to our conclusions if we take L_n always to be determined by eqn (1.1).

We suppose the cross-field thermal diffusivity takes the form

$$\chi_\perp = \frac{\chi_0 T^\alpha}{L_{p,T,n}^\gamma} \quad , \quad \chi_0 \propto n^\delta q^\mu R^\nu a^\sigma B^\rho \tag{3.1}$$

assuming $L_\parallel \sim Rq$. We use the parallel and perpendicular energy balance equations[27]

$$-n\chi_\parallel \nabla_\parallel T = \frac{B}{B_p}\frac{P}{2\pi\Delta_h R} \tag{3.2}$$

and

$$\frac{n\chi_\perp T_b}{\Delta_T} = \frac{P}{4e\pi^2 aR} \tag{3.3}$$

where B and B_p are the total and poloidal magnetic fields, subscript b denotes the plasma surface and P is the total heat flow to one divertor leg. The numerical coefficient $1/e$ is introduced to denote that the average temperature gradient length, Δ_T, is evaluated at the position of the $1/e$ fall-off of the radial heat flux, while the heat channel width, Δ_h, and Δ_T are considered to be proportional and characterised by Δ. Furthermore we suppose

$$\chi_\parallel = \chi_{\parallel 0} T^\beta \tag{3.4}$$

where $\beta = 5/2$ and $\chi_{\|0} \propto n^{-1}$ in the collisional region and $\beta = 1/2$ and $\chi_{\|0} \propto L_{\|} \sim Rq$ in the collisionless case.

As a result of eqns (3.1) to (3.4) (or directly from the stability criterion and eqn (3.2) for marginal stability models) we find the scalings

$$\Delta \propto n^{\lambda_n} R^{\lambda_R} a^{\lambda_a} B^{\lambda_B} q^{\lambda_q} P^{\lambda_P} \tag{3.5}$$

where, for the collisionless case (case I)

$$\begin{aligned} \lambda_n &= (3\delta - 2\alpha + 1)/u \\ \lambda_R &= 3(\nu + 1)/u \\ \lambda_a &= (3\sigma - 2\alpha + 1)/u \\ \lambda_B &= 3\rho/u \\ \lambda_q &= (3\mu + 2\alpha + 2)/u \\ \lambda_P &= (2\alpha - 1)/u \end{aligned} \tag{3.6}$$

with $u = 2\alpha + 3\gamma + 5$. For the collisional case with $L_n \sim L_T$ (case II), we find

$$\begin{aligned} \lambda_n &= 7(\delta + 1)/v \\ \lambda_R &= (7\nu + 2\alpha + 9)/v \\ \lambda_a &= (7\sigma - 2\alpha + 5)/v \\ \lambda_B &= 7\rho/v \\ \lambda_q &= (7\mu + 4\alpha + 4)/v \\ \lambda_P &= (2\alpha - 5)/v \end{aligned} \tag{3.7}$$

where $v = 2\alpha + 8\gamma + 9$. However, if we were to assume L_n is given by eqn (1.1) in the collisional case (case III),

$$\begin{aligned} \lambda_n &= 7(\gamma + 2\delta + 2)/2\omega \\ \lambda_R &= (7\nu + 2\alpha + 3\gamma/2 + 9)/\omega \\ \lambda_a &= (7\sigma - 2\alpha + 2\gamma + 5)/\omega \\ \lambda_B &= 7\rho/\omega \\ \lambda_P &= (2\alpha - 2\gamma - 5)/\omega \end{aligned} \tag{3.8}$$

where $\omega = 2\alpha + 5\gamma + 9$.

In Table 1 we group and classify the theoretical models in Section 2. Each group in column 1 (ie A, B, ...) is given a 'physics' label in column 2 and the models in Section 2 which fall within that group are listed in column 3 according to their equation numbers. Columns 4 - 10 specify the exponents $\alpha, \gamma, \delta, \mu, \nu, \sigma, \rho$. In Table 2 we list the values of λ_n, λ_R, λ_a, λ_B, λ_q, λ_P for cases I, II and III, under each group of models A-Q.

The models we have investigated belong to particular classes of physical processes. It is possible to establish more general constraints on the exponents in scaling (3.5) using scale

invariance or dimensional analysis[29,30]. Thus, if one supposes the anomalous transport processes are controlled by purely plasma physics processes involving collisions and finite β effects, then

$$\frac{\Delta}{R} \propto (nR^2)^{\lambda_n}(BR^{5/4})^{\lambda_B}(PR^{3/4})^{\lambda_P}\epsilon^{\lambda_\epsilon}q^{\lambda_q} \tag{3.9}$$

ie

$$\lambda_R + \lambda_a = 2\lambda_n + \frac{5}{4}\lambda_B + \frac{3}{4}\lambda_P + 1 \tag{3.10}$$

Alternatively, if one allows atomic physics processes to participate, but relaxes the need to involve the plasma pressure parameter β, then one can still obtain a constraint[31]

$$\frac{\Delta}{R} \propto (nR)^{\lambda_n}(BR)^{\lambda_B}(P/R)^{\lambda_P}\epsilon^{\lambda_\epsilon}q^{\lambda_q} \tag{3.11}$$

ie

$$\lambda_R + \lambda_a = \lambda_n + \lambda_B - \lambda_P + 1 \tag{3.12}$$

Comparisons are made between the scalings in Table 2 and experimental data from the COMPASS-D, Alcator C-MOD and JET tokamaks, using case I, II or III formulae as appropriate. Preliminary comparisons with theoretical models appeared in Ref 28.

For each scaling, scatter graphs of the predicted SOL widths against the experimental values are plotted. A linear fit to the data is formed, minimising the RMS deviation in both axes and allowing for estimates of experimental errors (both in the measurement of the SOL width and in the parameters in which the scalings are expressed). Since the scalings do not allow for any off-set, the linear fit is constrained to pass through the origin and is weighted to account for grouping of the experimental data in parameter space. The various scalings are compared for each tokamak using the minimised RMS deviation as a quality of fit parameter.

3.2 COMPASS-D data

Upstream SOL power width data from COMPASS-D L-mode discharges are compared with theoretical predictions for Δ from the scalings listed in Table 2. Since COMPASS-D operates with a SOL in the collisionless regime (typically $\nu_* = 0.25 - 4$), the case I formulae are used. As can be seen from Fig 1, model J and, to a lesser extent, models D and O provide substantially better fits to the data than the remainder, followed by models B1 and B2.

Figure 2 shows the COMPASS-D SOL power width data against scalings for models J, D and O together with the best-fit lines. It should be noted that models D and O lead to the same predictions for Δ and are thus indistinguishable.

3.3 JET and Alcator C-MOD data

Similar comparisons for JET[32] and Alcator C-MOD data[33,34] are performed. Since these two devices both exhibit a collisional SOL (JET has ν_* in the range 20 - 90, Alcator C-MOD in the range 40 - 180), the case II and III formulae are used, as appropriate. For the Alcator C-MOD data, models D and O and, to a lesser extent, models M, J and Q stand out as the best fits, as can be seen in Fig 1. In the JET case, Fig 1 shows models M, D and O and J provide notably better fits than the other models. Significantly, there is a substantial overlap of the best fitting models, not only between the two collisional devices but also with COMPASS-D.

Figure 3 shows the Alcator C-MOD power width data against scalings for models D and O, M and J, together with the best-fit lines. Figure 4 shows similar comparisons of the JET data with scalings for models M, D and O and J.

4 Comparisons of theoretical predictions for $\chi_\perp$ with JET and Alcator C-MOD data

A direct comparison of the models in Table 1 with radial profiles of $\chi_\perp$ in the SOL obtained in JET and Alcator C-MOD is also made, using the same method employed above in comparing the theoretical predictions for SOL widths. This data is obtained using onion skin models, which assume local power balances in each flux tube in the SOL. That used for JET is the DIVIMP onion-skin model[35] which relies on density and temperature measurements at the divertor surfaces; in fact, a modified form which includes convection with $D_\perp = 0.4\chi_\perp$ but assumes $T_i = T_e$ at the target, is employed here. In the case of the Alcator C-MOD analysis[33,34], the upstream density and temperature measurements are used directly, and folding into the divertor plate measurements allows an estimate of the effect of radiation to be made; again $D_\perp = 0.4\chi_\perp$ is assumed.

For the JET data, Fig 5 shows that model I provides the best fit, followed by models H, M, C, D and O. Results from JET with model I have previously been presented in Ref 36. For Alcator C-MOD, Fig 5 demonstrates that models D, O, N and I stand out from the rest as the best fits. Again, it is significant that the data from both devices supports several of the same models and that scalings derived from these models, in many cases, also provide the best fits to the SOL width data.

Figures 6 and 7 show the JET $\chi_\perp$ data against model I and the Alcator C-MOD $\chi_\perp$ data against models D and O, N and I, together with the best-fit lines to each data set.

5 Discussion

The comparison of theoretical SOL widths with collisionless COMPASS-D L-mode data indicates the best three models for cross-field transport in the SOL are, in decreasing order of success:

(i) model J (drift wave with collisionless skin-depth), which predicts

$$\Delta \propto (Rq)^{1/3} n^{-1/3} \tag{5.1}$$

(ii) model D (collisionless MHD interchange near $\beta_{\rm crit}$) or model O (collisionless skin-depth), which predict

$$\Delta \propto n^{-1/2} \tag{5.2}$$

The best free fit has

$$\Delta \propto q^{0.45} P^{0.14} n^{-0.44} B^{-0.17} \quad (R, a \text{ not varied}) \tag{5.3}$$

and is broadly consistent with eqns (5.1, 5.2). If one can establish a fit to Δ on one machine, then dimensional constraints, eg eqns (3.10) or (3.12), can be used to determine size scalings. For instance, combining the empirical scaling (5.3) from COMPASS-D with the plasma physics constraint (3.10), one finds $\Delta \propto R^{0.06}$ at fixed ϵ; alternatively eqn (3.12) implies $\Delta \propto R^{0.25}$.

The comparison with Alcator C-MOD and JET collisional data results in a significant overlap; with the equivalent ordering, it leads to

(i) model D (collisionless MHD interchange near $\beta_{\rm crit}$) or model O (collisionless skin-depth), which predict

$$\Delta \propto R^{3/10} a^{2/5} q^{-1/10} P^{-2/5} \tag{5.4}$$

(ii) model M (charge-exchange), which predicts

$$\Delta \propto R a^{2/5} q^{3/5} P^{-2/5} \tag{5.5}$$

(iii) model J (drift wave with collisionless skin-depth), which predicts

$$\Delta \propto R^{10/17} a^{4/17} q^{6/17} P^{-4/17} \tag{5.6}$$

for the Alcator C-MOD data, and

(i) model M (charge-exchange)

(ii) model D (collisionless MHD interchange near $\beta_{\rm crit}$) or model O (collisionless skin-depth)

(iii) model J (drift wave with collisionless skin-depth)

for the JET data.

It is interesting to convert the free fit scalings for the Alcator C-MOD SOL pressure scale length, Δ_p, associated with Fig 8 of Ref 34 to a similar form. In the 'open bypass' case

$$\Delta_p \propto R^{0.22} a^{0.94} q^{-0.72} n^{1.3} P^{-0.94} \tag{5.7}$$

while for the 'closed bypass' case

$$\Delta_p \propto R^{0.42} a^{0.67} q^{-0.25} n^{1.1} P^{-0.67} \tag{5.8}$$

While some of the exponents in eqns (5.7, 5.8) are broadly consistent with the best fits to the theoretical models, others (eg that on n; indeed these best fits are independent of n) are not. This might result from colinearities in the variables, which is not an issue when testing theory models. One should also note that the scalings (5.7) and (5.8) do not satisfy the constraints (3.10) or (3.12).

It is noteworthy that none of the data for the three tokamaks examined shows any sign of dependence on B, as would be expected from Bohm transport, a choice often used in edge modelling codes.

These best-fit results can be used to predict the mid-plane SOL widths in MAST and ITER. (The SOL widths will be larger at the divertor plates by a factor depending on the divertor geometry.) For the collisionless MAST case, eqns (5.1 - 5.2) provide the following estimates for $\Delta_{\rm MAST}$.

Model J : 5.7mm
Model D/O : 5.1mm

The constant of proportionality used to make these estimates is based on a weighted average of COMPASS-D data and data from the START tokamak (not presented here), which has a similar geometry to MAST. In the collisional ITER case, eqns (5.4 - 5.6) lead to the following predictions for $\Delta_{\rm ITER}$, where the constant of proportionality is now derived from a weighted average of the JET and Alcator C-MOD data.

Model D/O : 1.6mm
Model M : 4.1mm
Model J : 3.6mm

The errors in these predictions for MAST and ITER can correspond to upto a factor 2 in Δ, typically.

The large negative exponent of P in the scalings for Δ makes extrapolation from JET (with $P < 4$MW) and Alcator C-MOD ($P < 1$MW) to ITER (with $P \sim 100$MW) potentially subject to large errors, say a factor 2 in Δ. Nevertheless, the mean predictions for ITER from the simple zero-dimensional model for Δ correspond to rather narrow SOL widths, < 5mm.

The use of such scalings to extrapolate to ITER also raises the question of whether new processes intervene and invalidate the prediction. Physically it is more appropriate to discuss this in the context of dimensionless variables ($\rho_* = \rho_s/a$, the normalised Larmor radius, β and ν_*, or possibly λ_{cx}/a, the normalised charge-exchange mean free path) rather than engineering variables like n, B, R and P. The extrapolation in ν_* from collisional devices like JET is modest; those in β and ρ_* are more significant. Since ITER will have lower β, this is unlikely to change our conclusions as most of the best models are not dependent on finite β. The ρ_* scaling of Δ follows from the ρ_* scaling of $D_\perp$: if $D_\perp \propto \rho_*^n D_{\text{Bohm}}$ (where $n = 0$ for Bohm and $n = 1$ for gyro-Bohm diffusion), then eqns (1.1) and (1.2) imply $\Delta/R \propto \rho_*^{(n+1)/2}$. Whereas one might expect a Bohm-like scaling to change to gyro-Bohm as ρ_* decreases, the converse is unlikely and most of the models considered are gyro-Bohm in character (the relevance of model M, involving atomic physics processes, would only change if the parameter λ_{cx}/ρ_s varied greatly in the extrapolation and this is not the case). However, a change in scaling with ρ_* might become relevant if the extrapolated Δ approached a microscopic distance like ρ_s.

The comparisons with experiment and predictions for MAST and ITER have been based on simple power law scalings; this is a consequence of using theoretical models for cross field transport which are based on a single process and specifying the collisionality regime for classical parallel transport. It could be the case that one or more transport processes are operating simultaneously, leading to a more complex functional form for the dependence of Δ on the SOL parameters. While this situation would be difficult to detect and analyse in the data, we can take comfort from the fact that the favoured models have been compared over a wide range of parameters from COMPASS-D, JET and Alcator C-MOD.

Some points remain that require further investigation. Fits to the COMPASS-D database are strongly influenced by a relatively small number of points with extreme values of SOL width (either narrow or wide). In addition the database is currently limited to L-mode shots. Thus shots are needed to populate further the extremes of the database. This should involve operating at high and low edge densities as well as including H-mode shots. Similarly, the inclusion of lower power shots in the JET database would be helpful in increasing the range of Δ for that device. The comparisons of SOL widths lead to a different ordering of the preferred models for Alcator C-MOD and JET although a substantial overlap does exist. Furthermore, the direct comparisons of theoretical models for $\chi_\perp$ with onion-skin model derived values for these two machines indicate other models, particularly model I for JET, provide possible descriptions of the SOL transport, although again there is some overlap

with those leading to the best fits for Δ.

6 Conclusions

The extensive data in the scalings of SOL power widths Δ with plasma parameters (eg n, P, B, R, a); available from COMPASS-D, JET and Alcator C-MOD has provided an opportunity to test a wide range of theoretical models for SOL transport. These models, based on cross-field thermal diffusivities or marginally stable (or 'preferred'), SOL profiles, were summarised in Section 2. In Section 3.1, the implications of these models for the scalings of Δ were derived, using simple SOL balances perpendicular and parallel to the magnetic field for the cases of a collisionless and collisional SOL. Comparisons of these predictions were made with the collisionless SOL scalings from COMPASS-D in Section 3.2 and with the collisional SOL scalings from JET and Alcator C-MOD in Section 3.3. Significantly, the data from both JET and Alcator C-MOD favoured the same small group of models; collisional MHD interchange near β_{crit} (D), collisionless skin-depth (O), charge-exchange (M) and drift wave with collisionless skin-depth (J). Models D, O and M were also favoured in direct analysis of $\chi_\perp$ from the two devices, together with model I (drift wave with collisional skin-depth) which provided the best fit for JET. In addition, collisionless SOL scalings for three of these models, D, O and J also provided good fits to the COMPASS-D data. Thus, although the fits were not always very good, the same models consistently tended to perform best over a wide range of conditions, providing support for their validity.

The preferred transport models, none of which showed any scaling with B, were used to provide predictions of Δ at the mid-plane for MAST (a collisionless SOL), and for ITER (a collisional SOL) where the resulting rather small values are in part due to an adverse scaling with power.

Acknowledgements

The authors acknowledge the encouragement of Dr D C Robinson on this topic and valuable comments by Drs S Krashenninikov, P Catto, P Helander and H Wilson. The JET data was obtained under a JET Task Agreement between JET and UKAEA Fusion. This work was funded jointly by the UK Department of Industry and Euratom; one of the authors (B La Bombard) was supported by US Department of Energy Contract No DEA CO2-78 ET5 103 and another (K Morel) by a UK Engineering and Physics Science Research Council Grant No 96305109.

References

1 G F Matthews, Journal of Nuclear Materials **220 - 222** 104 (1995)

2 G P Maddison, P C Stangeby and C S Pitcher, in Theory of Fusion Plasmas (eds J W Connor, E Sindoni and J Vaclavik), Editrice Compositori, Bologna (1997) 59

3 A V Nedapasov, Soviet Journal of Plasma Physics **15** 659 (1989)

4 X Garbet et al, Nuclear Fusion **31** 967 (1991)

5 W Kunkel and J Guillory, in Phenomena in Ionised Gases (Proc 7th Conf, Belgrade, 1965) Grad Jevinska Kniga Belgrade (1966) Vol **1** 702

6 Y-K M Peng et al, in Plasma Physics and Controlled Nuclear Fusion Research (Proc 15th Int Conf, Seville, 1994) IAEA Vienna 1996 Vol **2** 643

7 O P Pogutse and W Kerner, in Proc 21st EPS Conference on Controlled Fusion and Plasma Physics, Montpellier, 1994, Geneva Part **II** 882

8 W Kerner, O P Pogutse and R Van der Linden, Plasma Physics and Controlled Fusion **39** 757 (1997)

9 M Endler et al, Nuclear Fusion **35** 1307 (1995)

10 O P Pogutse et al, Plasma Physics and Controlled Fusion **36** 1963 (1994)

11 J G Cordey, W Kerner and O Pogutse, Plasma Physics and Controlled Fusion **37** 773 (1995)

12 J G Cordey et al, Plasma Physics and Controlled Fusion **38** 1905 (1996)

13 Yu A Tsidulko, H L Berk and R H Cohen, Physics of Plasmas **1** 1199 (1994)

14 J R Myra, D A D'Ippolito and J P Goedbloed, Physics of Plasmas **4** 1330 (1997)

15 S V Novakovskii et al, Physics of Plasmas **2** 781 (1995)

16 A Zeiler et al, Physics of Plasmas **3** 2951 (1996)

17 A Zeiler, D Biskamp and J R Drake, Physics of Plasmas **3** 3947 (1996)

18 A Zeiler, J R Drake and D Biskamp, Physics of Plasmas **4** 991 (1997)

19 S V Novakovskii et al, Physics of Plasmas **2** 3764 (1995)

20 A V Chankin, Plasma Physics and Controlled Fusion **39** 1059 (1997)

21 B B Kadomtsev and O P Pogutse, in Plasma Physics and Controlled Nuclear Fusion Research (Proc 11th Int Conf, Kyoto, 1986) IAEA Vienna 1987 Vol **2** 69

22 O Pogutse et al, in Proc 24th EPS Conference on Controlled Fusion and Plasma Physics, Berchtesgaden, 1997, Geneva Part **III** 1041

23 H L Berk, D D Ryutov and Yu Tsidulko, JETP Letters **52** 674 (1990); Physics of Fluids B**3** 1346 (1991)

24 H L Berk et al, Nuclear Fusion **33** 263 (1993)

25 X Q Xu, Physics of Fluids B**5** 3641 (1993)

26 N Mattor and R H Cohen, Plasma Physics and Controlled Fusion **36** 1115 (1994)

27 S-I Itoh and K Itoh, Plasma Physics and Controlled Fusion **36** 1845 (1994)

28 G F Counsell et al, Proc 24th EPS Conference on Controlled Fusion and Plasma Physics, Berchtesgaden, 1997, Geneva Part **I** 253

29 J W Connor and J B Taylor, Nuclear Fusion **17** 1047 (1977)

30 B B Kadomtsev, Soviet Journal of Plasma Physics **1** 295 (1975)

31 K Lackner, Comments on Plasma Physics and Controlled Fusion **15** 359 (1994)

32 S K Erents et al, Journal of Nuclear Materials **241-243** 433 (1997)

33 B La Bombard et al, Journal Nuclear Materials **241-243** 149 (1997) (Fig 8 of this reference shows a regression analysis of some of the dataset used here)

34 B La Bombard et al, in Fusion Energy (Proc 16th Conf, Montreal, 1996) IAEA Vienna 1997 Vol **I** 825

35 P C Stangeby and J D Elder, Nuclear Fusion **35** 1391 (1995)

36 S K Erents et al, in Proc of 24th EPS Conference on Controlled Fusion and Plasma Physics, Berchtesgaden, 1997, Geneva, Part **I** 121

Table 1

Group	Physics	Equations	α	γ	δ	μ	ν	σ	ρ
A	Marginal Ideal MHD	2.5	-	-	-	-	-	-	-
B1	Endplate MHD interchange; L_p	2.12 2.13 2.18 2.19 ($\nu = 0$)	3/2	1	0	1	0	0	-2
B2	with L_n	2.41	3/2	1	0	1	0	0	-2
C	Collisionless MHD interchange	2.14 2.19($\nu = 1$)	5/2	2	1	3	1	0	-4
D	Collisionless MHD interchange near β_{crit}	2.15	1/2	0	-1	-1	-1	0	0
E1	Resistive MHD interchange; L_p	2.13 2.16 2.17	-1/2	1	1	2	1	0	-2
E2	with L_n	2.32	- 1/2	1	1	2	1	0	-2
F	Drift	2.20	3/2	4/3	0	1/3	1/3	0	-2
G1	MHD interchange	2.21	1	1	0	0	0	0	-2
G2	End plate MHD	2.22	4/3	4/3	0	1/3	1/3	0	-2
G3	Axial flow shear	2.23	3/2	1	0	0	0	0	-2
H	Drift	2.37	- 11/6	8/3	5/3	10/3	10/3	0	-2
I	Drift with collisional skin-depth	2.42	-3/2	0	0	0	0	0	0
J	Drift with collisionless skin-depth	2.46	1/2	1	-1	0	0	0	0
K1	Drift Alfvén low collisionality	2.47	3/2	3/2	0	1/2	1/2	0	-2
K2	Drift Alfvén higher collisionality	2.48	5/6	4/3	1/3	2/3	2/3	0	-2
L1	∇T_e sheath mode	2.52 2.59	3/2	4/3	0	1/3	1/3	0	-2
L2	Minimum enstrophy	2.68	3/2	0	0	-1	-1	0	-2
L3	Canonical profile	2.64	-	-	-	-	-	-	-
M	Charge-exchange	2.69	1/2	0	-1	0	0	0	0
N	Bohm	2.70	1	0	0	0	0	0	-1
O	Collisionless skin-depth	2.71	1/2	0	-1	-1	-1	0	0
P	Dimensional estimate	2.72	-	-	-	-	-	-	-
Q	Constant	2.73	0	0	0	0	0	0	0

Table 2

Group	Case	λ_n	λ_R	λ_a	λ_B	λ_q	λ_P
A	I	1/5	3/5	-2/5	-6/5	8/5	2/5
	II	7/9	1	-2/9	-14/9	2	2/9
B1	I	-2/11	3/11	-2/11	-6/11	8/11	2/11
	II	7/19	12/19	2/19	-14/19	17/19	-2/19
B2	II	7/19	12/19	2/19	-14/19	17/19	-2/19
	III	21/37	27/37	8/37	-28/37	33/37	-8/37
C	I	-1/16	3/8	-1/4	-3/4	1	1/4
	II	1/2	3/4	0	-1	5/4	0
D	I	-1/2	0	0	0	0	0
	II	0	3/10	2/5	0	-1/10	-2/5
E1	I	5/7	6/7	2/7	-6/7	1	-2/7
	II	14/15	1	2/5	-14/15	16/15	-2/5
E2	II	14/15	1	2/5	-14/15	16/15	-2/5
	III	35/17	33/17	16/17	-28/17	31/17	-16/17
F	I	-1/6	1/3	-1/6	-1/2	1/2	1/6
	II	21/64	43/64	3/32	-21/32	37/64	-3/32
G1	I	-1/10	3/10	-1/10	-3/5	2/5	1/10
	II	7/18	11/18	1/6	-7/9	4/9	-1/6
G2	I	-1/7	12/35	-1/7	-18/35	17/35	1/7
	II	1/3	2/3	1/9	-2/3	5/9	-1/9
G3	I	-2/11	3/11	-2/11	-6/11	5/11	2/11
	II	7/19	12/19	2/19	-14/19	10/19	-2/19
H	I	29/28	39/28	1/2	-9/14	25/28	-1/2
	II	7/9	43/36	13/36	-7/12	5/6	-13/36
I	I	2	3/2	2	0	-1/2	-2
	II	7/6	1	4/3	0	-1/3	-4/3
J	I	-1/3	1/3	0	0	1/3	0
	II	0	10/17	4/17	0	6/17	-4/17

Table 2 continued

Group	Case	λ_n	λ_R	λ_a	λ_B	λ_q	λ_P
K1	II	14/45	31/45	4/45	-28/45	6/10	-4/45
	III	21/45	23/15	1/6	-7/10	6/10	-1/6
K2	II	49/78	71/78	10/39	-28/39	51/78	-10/39
	III	84/95	104/95	36/95	-84/95	68/95	-36/95
L1	I	-1/6	1/3	-1/6	-1/2	1/2	1/6
	II	21/64	43/64	3/32	-21/32	37/64	-3/32
L2	I	-1/4	0	-1/4	-3/4	1/4	1/4
	II	7/12	5/12	1/6	-7/6	1/4	-1/6
L3	I	0	0	-1/4	-3/4	1/4	1/4
	II	0	0	-1/4	-3/4	1/4	1/4
M	I	-1/2	1/2	0	0	1/2	0
	II	0	1	2/5	0	3/5	-2/5
N	I	-1/7	3/7	-1/7	-3/7	4/7	1/7
	II	7/11	1	3/11	-7/11	8/11	-3/11
O	I	-1/2	0	0	0	0	0
	II	0	3/10	2/5	0	-1/10	-2/5
P	I	-1/7	3/7	-1/7	-3/7	4/7	1/7
	II	0	8/15	-1/15	-7/15	3/5	1/15
Q	I	1/5	3/5	1/5	0	2/5	-1/5
	II	7/9	1	5/9	0	4/9	-5/9

Figure Captions

Figure 1 Normalised RMS deviation for all models (in order of decreasing quality of fit) for SOL width data from COMPASS-D, Alactor C-MOD and JET

Figure 2 COMPASS-D SOL power width data against scalings for models J, D and O together with the best-fit line

Figure 3 Alcator C-MOD power width data against scalings for models D, O, M and J together with the best-fit line

Figure 4 JET data against scalings for models M, D and O and J together with the best-fit line

Figure 5 Normalised RMS deviation for all models (in roder of decreasing quality of fit) for Onion-Skin Model $\chi_\perp$ data from JET and Alcator C-MOD

Figure 6 JET $\chi_\perp$ data against model I together with the best-fit line

Figure 7 Alcator C-MOD $\chi_\perp$ data against models D, O, N and I together with the best-fit line

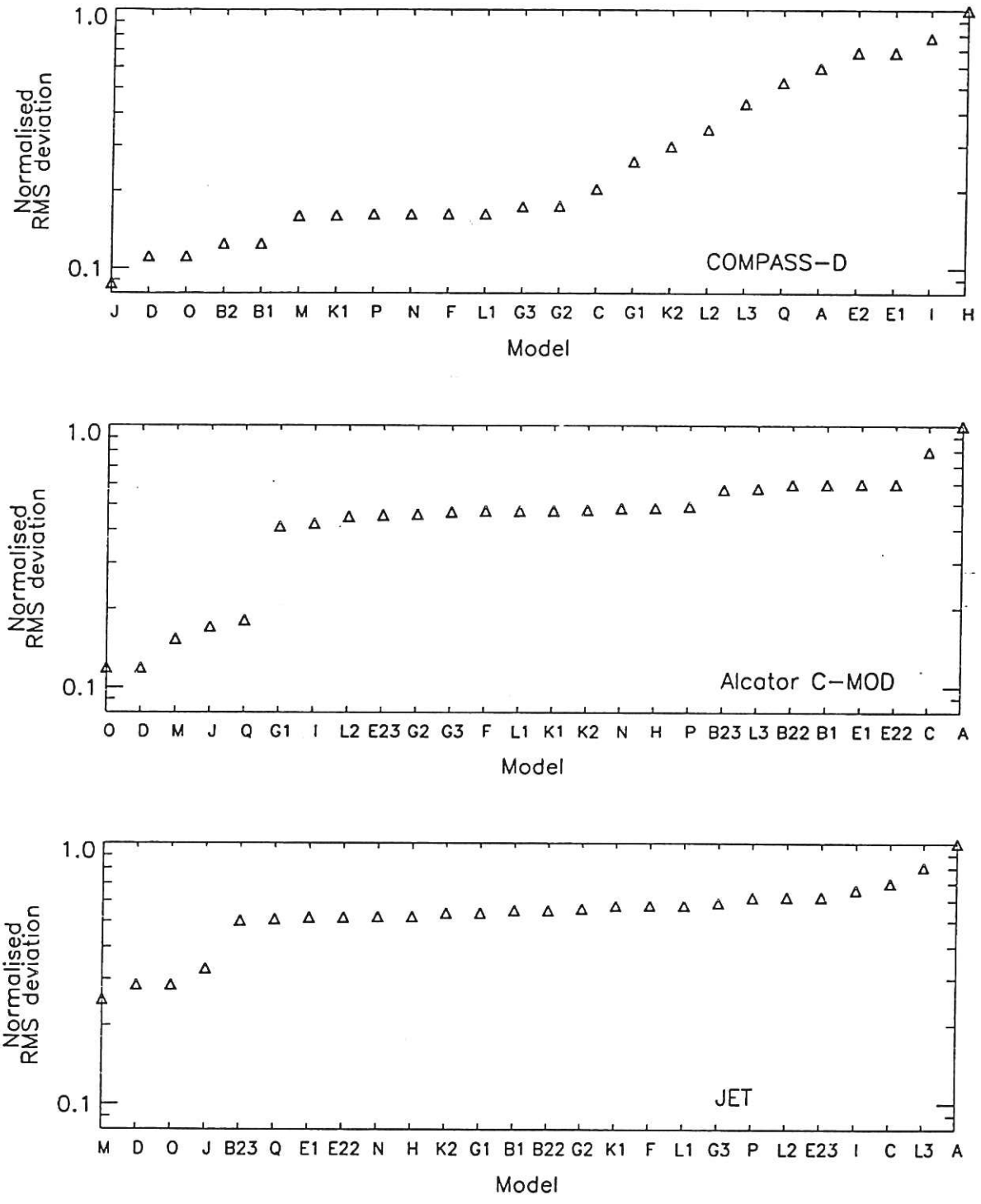

Figure 1 Normalised RMS deviation for all models (in order of decreasing quality of fit) for SOL width data from COMPASS-D, Alcator C-MOD and JET

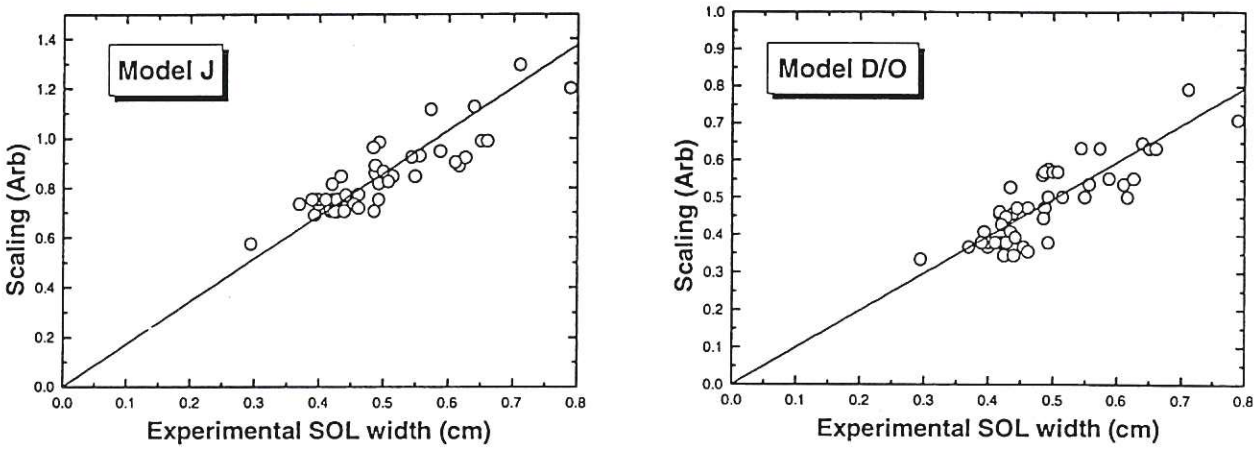

Figure 2 COMPASS-D SOL power width data against scalings for models J, D and O together with the best-fit line

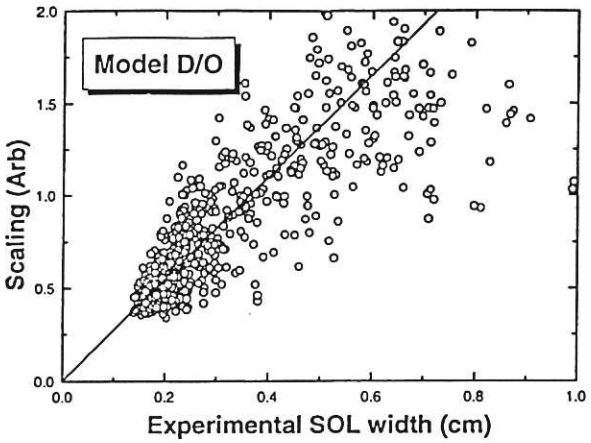

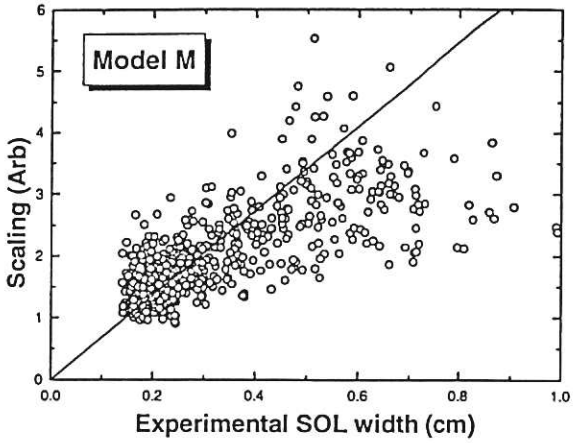

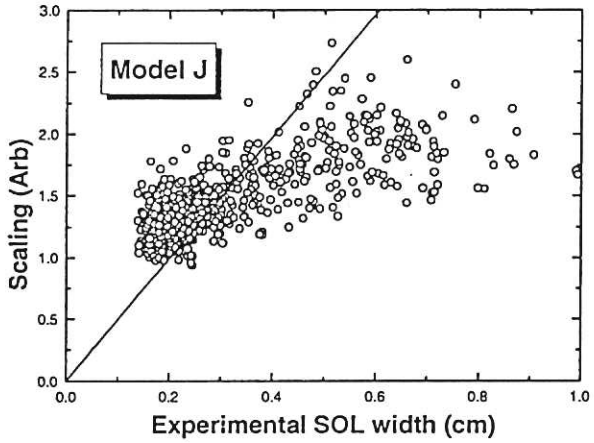

Figure 3 Alcator C-MOD power width data against scalings for models D, O, M and J together with the best-fit line

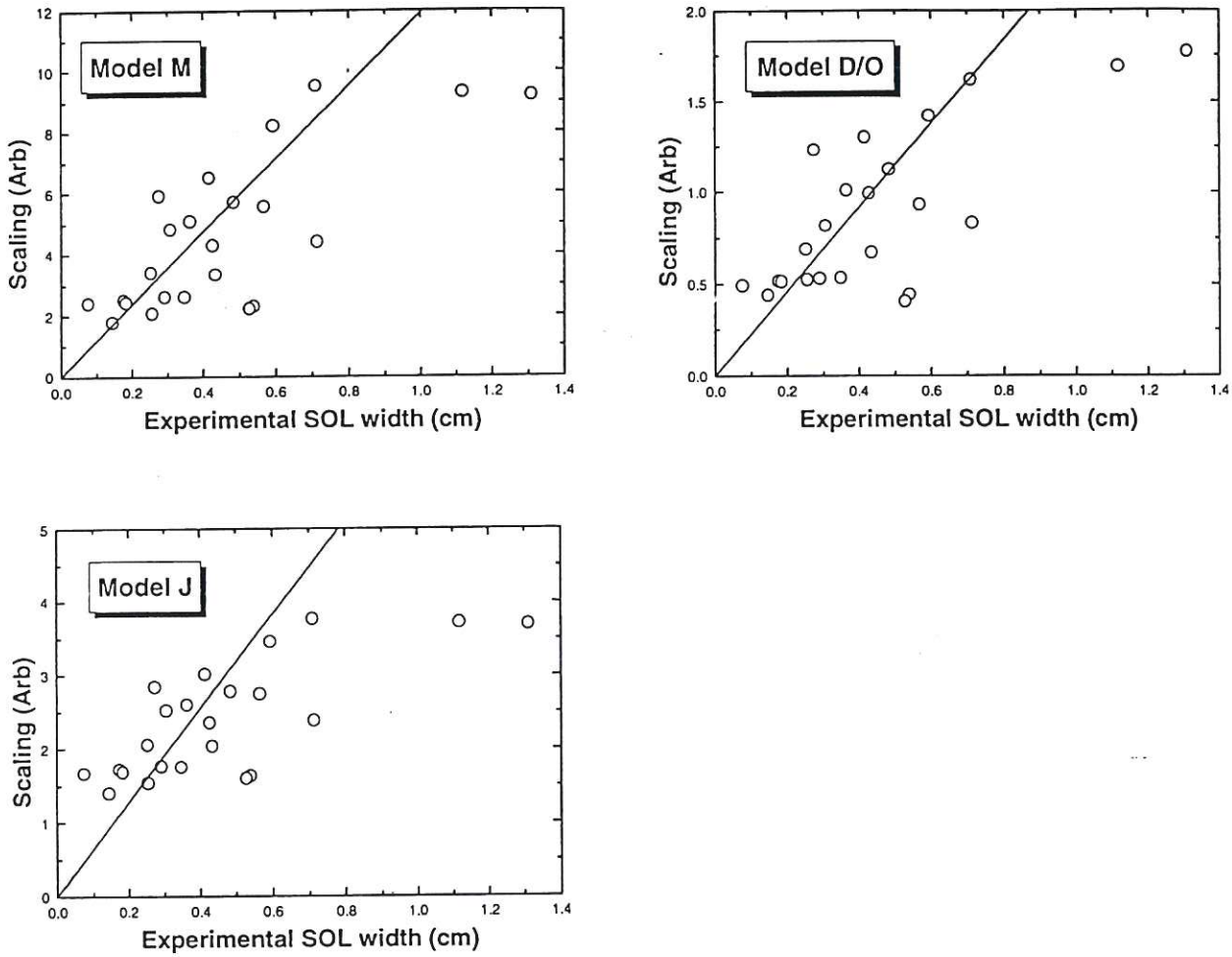

Figure 4 JET data against scalings for models M, D and O and J together with the best-fit line

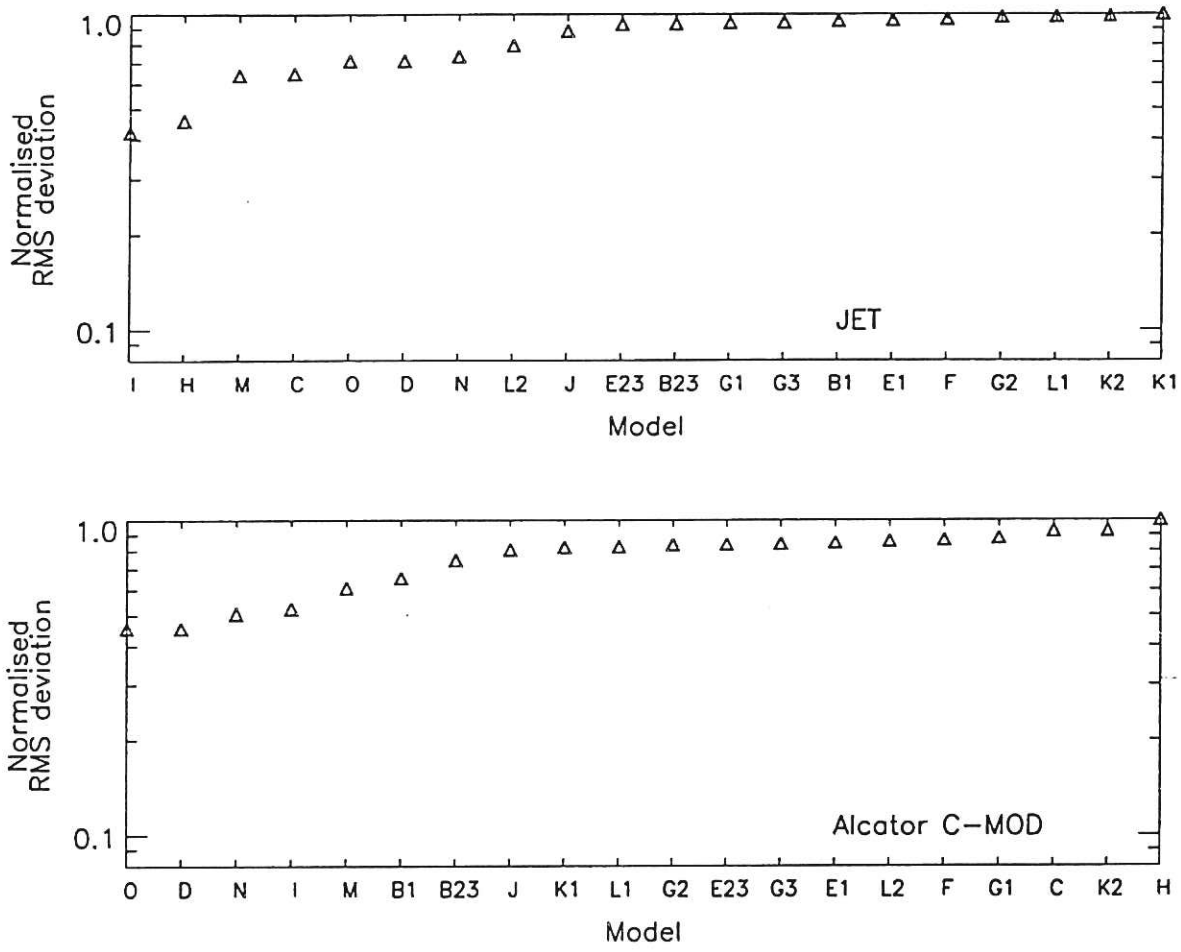

Figure 5 Normalised RMS deviation for all models (in order of decreasing quality of fit) for Onion-Skin Model $\chi_{\perp}$ data from JET and Alcator C-MOD

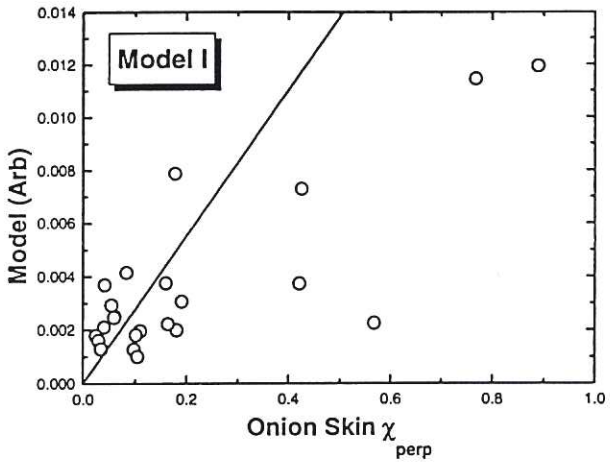

Figure 6 JET $\chi_{\perp}$ data against model I together with the best-fit line

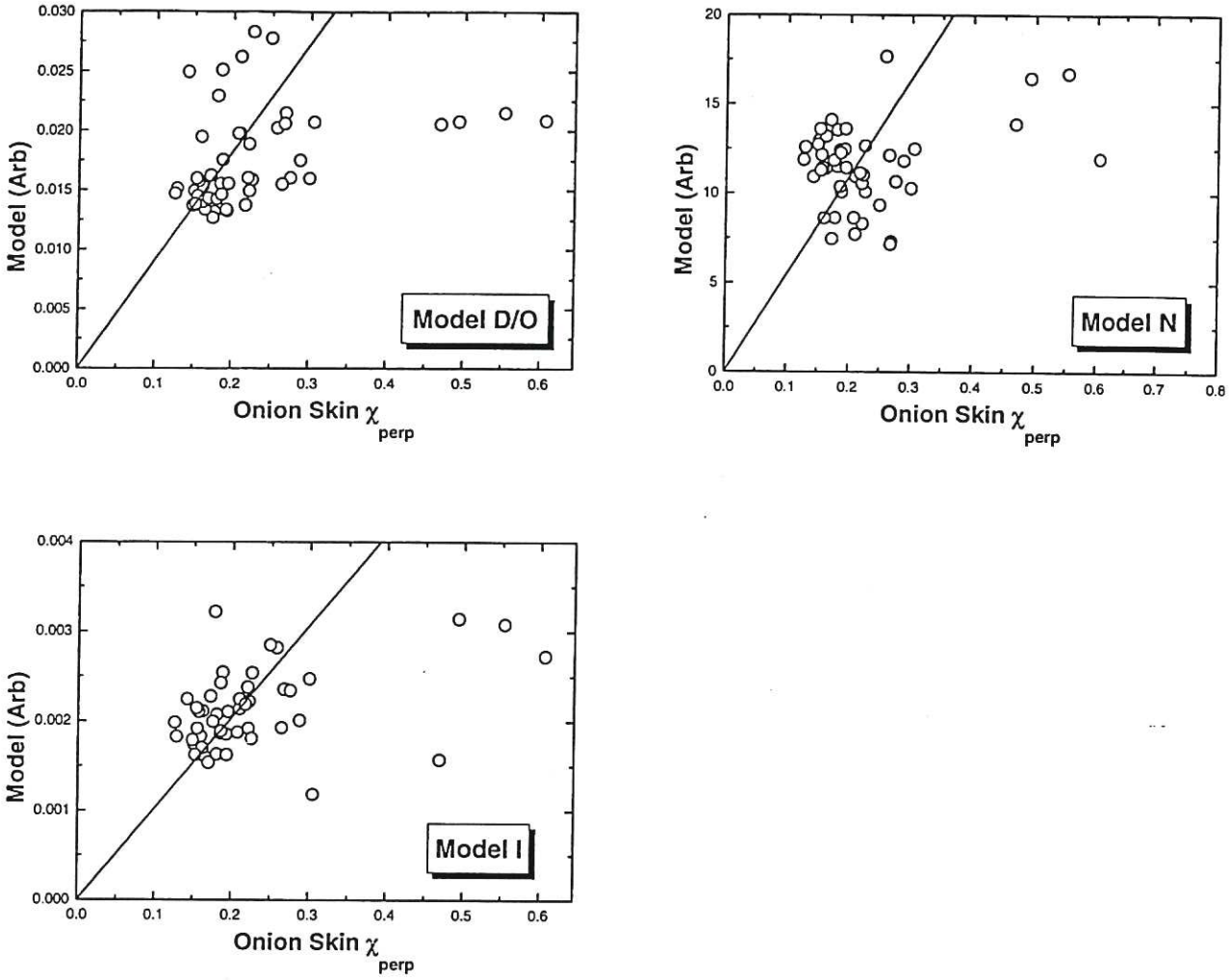

Figure 7 Alcator C-MOD $\chi_{\perp}$ data against models D, O, N and I together with the best-fit line